photonics

MDPI

Article

Stark Effect and Valley Polarization of Interlayer Excitons in 3° Twisted Bilayer WSe_2

Haohan Zhou [1,2,*] and Koustav Pal [2]

[1] School of Physics and Optoelectronics, South China University of Technology, Guangzhou 511442, China
[2] Spin-X Institute, South China University of Technology, Guangzhou 511442, China; koustav.pal97@gmail.com
* Correspondence: phzhh@mail.scut.edu.cn

Abstract

Twist-angle engineering in van der Waals bilayers enables excitonic and valley phenomena that are not accessible in naturally stacked crystals. In a dual-gated 3° twisted bilayer WSe_2 device, low-temperature polarization-resolved photoluminescence spectroscopy reveals a pronounced Stark shift of the interlayer exciton, yielding an effective electron–hole separation of 0.26 nm and indicating a strongly hybridized interlayer excitonic state. The degree of circular polarization (DOCP) is strongly doping-dependent but only weakly affected by the vertical electric field: at zero magnetic field, the DOCP is about 30% in the electron-doped regime and about 18% in the hole-doped regime. An out-of-plane magnetic field of 9 T sharpens this contrast to about 35% and 13%, respectively, suggesting distinct intervalley depolarization dynamics in the two doping regimes. Together, these results show that an electric field primarily tunes exciton energy, whereas doping and a magnetic field control valley polarization, highlighting small-angle twisted bilayer WSe_2 as a promising platform for tunable excitonic and valley-optoelectronic functionalities.

Keywords: twisted bilayer WSe_2; interlayer exciton; stark effect; valley polarization

1. Introduction

Van der Waals (vdW) heterostructures have established a powerful platform for engineering electronic and optical phenomena in atomically thin materials through stacking sequence, layer composition, and rotational alignment. In particular, twist-angle control has unlocked moiré superlattices and the broader field of twistronics, where electronic states can be precisely tailored without any chemical modification of the constituent layers [1–4]. In semiconducting transition metal dichalcogenide (TMD) bilayers, small twist angles generate long-wavelength moiré potentials that strongly reconstruct the electronic and excitonic landscape, giving rise to localized excitons, modified valley selection rules, and tunable light–matter interactions [5–10]. Twisted bilayer WSe_2 has further emerged as a key semiconductor moiré platform for correlated electronic phases—from flat-band formation to unconventional superconductivity and Mott insulating behavior—underscoring the broader importance of its angle-dependent electronic structure [11–13].

Interlayer excitons in bilayer TMDs are particularly compelling quantum objects: with the electron and hole spatially separated across opposite layers, they acquire a permanent out-of-plane electric dipole moment, pronounced Stark tunability, and exceptionally long radiative lifetimes [14–16]—properties that render them attractive for excitonic and valleytronic device applications. In bilayer WSe_2, both experiments and theory have demonstrated that low-energy interlayer excitons can be simultaneously spatially and

Check for updates

Received: 30 April 2026
Revised: 3 June 2026
Accepted: 11 June 2026
Published: 13 June 2026

Copyright: © 2026 by the authors. Licensee MDPI, Basel, Switzerland. This article is an open access article distributed under the terms and conditions of the Creative Commons Attribution (CC BY) license.

momentum-indirect, involving transitions between the Λ (or Q) and K/Γ valleys [7,17,18]. At small twist angles, enhanced interlayer coupling combined with moiré-driven band reconstruction is expected to further hybridize the layer and momentum-space characteristics of these excitons, yielding K-Q interlayer states with reduced effective electron–hole separation and unconventional Stark and valley responses [6,7,18].

Despite rapid advances in moiré exciton physics, the combined influence of vertical electric fields, electrostatic doping, and out-of-plane magnetic fields on interlayer excitons in the small-angle twisted bilayer WSe_2 regime remains poorly understood. Systematic experimental studies linking Stark tunability to valley polarization specifically at ∼3° are still absent. Here, we investigate a dual-gated 3° twisted bilayer WSe_2 device using low-temperature polarization-resolved photoluminescence spectroscopy under independent electric and magnetic field control. A pronounced linear Stark shift yields an effective electron–hole separation of only 0.26 nm, directly evidencing a strongly hybridized K-Q interlayer excitonic state. We further uncover a robust doping-dependent asymmetry in the degree of circular polarization (DOCP) that is amplified under a 9 T out-of-plane magnetic field, while remaining entirely insensitive to the vertical electric field. These results delineate the distinct functional roles of electric fields, carrier doping, and magnetic fields in controlling interlayer excitons and valley polarization, suggesting that the 3° twisted bilayer WSe_2 is a candidate system worthy of further investigation across multiple devices.

2. Experimental Details

2.1. Device Fabrication

The dual-gated twisted bilayer WSe_2 heterostructure was fabricated using mechanical exfoliation and dry-transfer assembly. Thin flakes of hexagonal boron nitride (hBN), few-layer graphene, and WSe_2 were exfoliated from bulk crystals (HQ Graphene) onto SiO_2/Si substrates. A viscoelastic stamp consisting of polydimethylsiloxane (PDMS), polypropylene carbonate (PPC), and polycarbonate (PC) was used to sequentially pick up and assemble the heterostructure. The two-dimensional materials to be stacked are first located under an optical microscope. The stamp is then positioned directly above the target material and slowly lowered until it contacts the silicon substrate. Upon contact with the silicon substrate, bright Newton's rings appear. The stamp is further lowered, allowing the Newton's rings to expand and cover the target sample. The stamp is then heated to enhance adhesion, cooled to an appropriate temperature, and lifted. During lifting, the Newton's rings slowly contract, and the sample is picked up. To achieve precise angular stacking, hexagonal boron nitride (hBN) is typically used as a cutting tool: the stamp first picks up an hBN flake, which is then used to cut other two-dimensional materials. The stamp with the hBN flake is positioned directly above the WSe_2. The stamp is lowered to allow the Newton's rings to slowly expand to the edge of the hBN. The stamp is then promptly lifted, causing the Newton's rings to contract, and the hBN edge extracts the WSe_2 that has come into contact. After lifting the stamp until the Newton's rings disappear, the sample stage is rotated to achieve a predetermined twist angle between the WSe_2 on the substrate and the WSe_2 already picked up. The stamp is lowered again to bring the two into contact, and the stack with the precise twist angle is picked up by the stamp through a heating–cooling process. The entire process is carried out in a glovebox to ensure cleanliness. A tear-and-stack procedure was employed to form a twisted WSe_2 homobilayer with a nominal twist angle of approximately 3°. The assembled stack was transferred onto a SiO_2/Si substrate pre-patterned with Ti/Au electrodes and released under mild heating to establish electrical contact between the graphene leads and the metal electrodes. Residual

polymer contamination was removed by sequential solvent cleaning in chloroform, acetone, and isopropanol.

The device adopts a dual-gate architecture in which the top and bottom few-layer graphene flakes serve as gate electrodes, while hBN layers act as high-quality dielectric spacers that fully encapsulate the twisted bilayer WSe_2. The carrier density n and the vertical displacement field D are controlled independently through the top- and bottom-gate voltages, V_t and V_b, according to

$$n = \frac{C_t(V_t - V_{t,0}) + C_b(V_b - V_{b,0})}{e}, \quad (1)$$

$$D = \frac{C_t(V_t - V_{t,0}) - C_b(V_b - V_{b,0})}{2}, \quad (2)$$

where C_t and C_b are the areal capacitances of the top and bottom hBN dielectric layers, respectively, and $V_{t,0}$ and $V_{b,0}$ denote the charge-neutrality offset voltages. When $C_t \approx C_b$, the symmetric combination $V_t + V_b$ predominantly controls n, while the antisymmetric combination $V_t - V_b$ predominantly controls D, enabling clean electrostatic decoupling of doping and field effects throughout the experiments.

2.2. Optical Measurements

Optical measurements were performed in a closed-cycle helium cryostat (attoDry2100) (Attocube Systems AG, Haar, Germany) with the sample temperature stabilized at $T = 2$ K. A continuous-wave 532 nm laser was used for above-gap excitation. The photoluminescence (PL) signal was collected through the same objective lens in a confocal back-scattering geometry and dispersed by a Princeton Instruments HRS300 spectrometer (Princeton Instruments, Acton, MA, USA) equipped with a charge-coupled device (CCD) detector. Throughout the experiment, the exciton peak position and linewidth did not exhibit significant drift, indirectly indicating the uniformity and stability of the sample. Data processing and figure generation were performed using Python 3.12 with standard scientific libraries, including NumPy, SciPy, pandas, and Matplotlib.

For polarization-resolved measurements, circularly polarized emission was analyzed using a quarter-wave plate (QWP), a half-wave plate (HWP), and a linear polarizer inserted into the collection path to selectively detect left-handed (σ^+) and right-handed (σ^-) circularly polarized light. The degree of circular polarization (DOCP) was defined as

$$\mathrm{DOCP} = \frac{I(\sigma^+) - I(\sigma^-)}{I(\sigma^+) + I(\sigma^-)}, \quad (3)$$

where $I(\sigma^+)$ and $I(\sigma^-)$ correspond to the PL intensity of the σ^+ and σ^- polarization components, respectively. For electric-field-dependent measurements, opposite gate voltages were applied to vary the vertical displacement field D while maintaining the device close to charge neutrality ($n \approx 0$). For doping-dependent measurements, both gates were swept with the same polarity to primarily vary the carrier density n at fixed D. Magnetic field measurements were performed in a superconducting magnet with the magnetic field direction perpendicular to the sample plane, reaching a maximum field strength of 9 T.

3. Results and Discussion

3.1. Device Structure and Excitonic Spectrum

Figure 1 summarizes the device architecture and the twist-angle-dependent modification of the excitonic spectrum. Figure 1a shows an optical microscope image of the nominal 3° twisted bilayer WSe_2 device. The well-defined flake outline and relatively uniform optical contrast suggest good optical homogeneity and the absence of obvious

large bubbles or wrinkles in the field of view. The device stack comprises a top graphene gate (Top Gr), top hBN dielectric, twisted bilayer WSe_2 (BL WSe_2), bottom hBN dielectric, and bottom graphene gate (Bottom Gr), with an additional middle graphene flake serving as a grounding contact, as indicated in the figure. Figure 1b illustrates the dual-gate device schematic, in which independent top- and bottom-gate voltages enable simultaneous and decoupled tuning of the carrier density n and the vertical displacement field D in the WSe_2 bilayer. At small twist angles, the lattice mismatch between the two WSe_2 layers generates a long-wavelength moiré superlattice potential that modulates the interlayer coupling in real space and reconstructs the electronic and excitonic structure of the bilayer. Such reconstruction can enhance the role of Q-valley conduction states in low-energy optical transitions and is consistent with the formation of hybridized K-Q intervalley interlayer excitons.

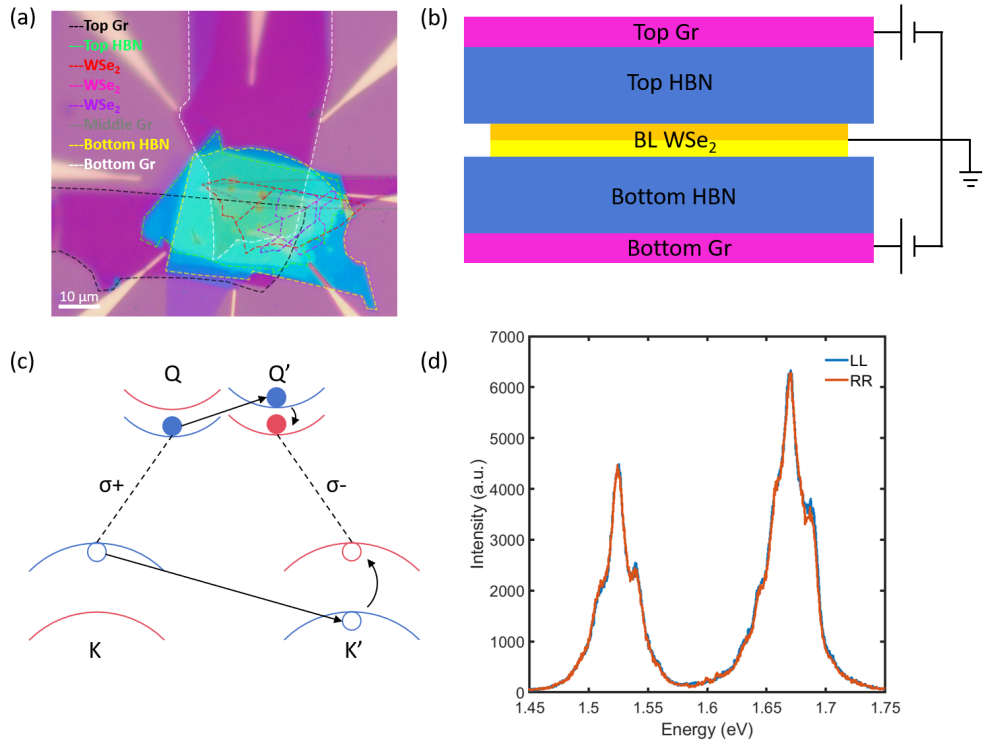


Figure 1. Device structure and excitonic spectrum of the nominal 3° twisted bilayer WSe_2 homobilayer. (**a**) Optical micrograph of the fabricated device. The scale bar in (**a**) is 10 μm. (**b**) Schematic of the dual-gated heterostructure comprising top and bottom graphene gates, hBN dielectric layers, and the twisted bilayer WSe_2. (**c**) Schematic illustration of valley-selective excitation and intervalley relaxation pathways relevant to circularly polarized emission in twisted bilayer WSe_2. The blue line represents spin-up, and the red line represents spin-down. The depolarization process requires both phonon-induced momentum transitions (straight arrows) and spin-flip transitions of the two carriers (curved arrows). (**d**) Co-circularly polarized photoluminescence spectra of the nominal 3° twisted bilayer WSe_2, showing the interlayer and intralayer excitonic emission features.

Figure 1c shows a schematic of the reconstructed band structure of twisted bilayer WSe_2. The Q- and Q′-valley conduction band states and the K- and K′-valley valence band states are each spin-split owing to strong spin–orbit coupling, with the detailed splitting governed by stacking configuration and interlayer hybridization [19]. Under σ^+ excitation, valley-selective optical selection rules create holes preferentially in the +K valley of the valence band, while the associated electrons occupy the Q-valley conduction band states, consistent with the K-Q hybrid interlayer exciton picture. In the absence of intervalley relaxation, emission would remain entirely in the σ^+ channel. In practice, intervalley scattering transfers a fraction of the population to the opposite valley, generating a finite

σ^- emission component. The DOCP therefore serves as a direct experimental proxy for the valley polarization retained over the exciton lifetime.

Figure 1d presents the polarization-resolved PL spectrum of the 3° twisted bilayer WSe_2 at $T = 2$ K, recorded under co-circular detection. Two dominant emission features are observed: a lower-energy peak near 1.50–1.55 eV assigned to the interlayer exciton and a higher-energy peak near 1.67–1.70 eV associated with intralayer excitonic emission. In natural bilayer WSe_2 with standard 2H stacking, strong interlayer coupling suppresses the intralayer exciton emission, leaving the spectrum dominated by interlayer transitions [15]. This stands in sharp contrast to the prominent intralayer exciton peaks observed in our small-angle twisted bilayer, which directly demonstrates the efficacy of twist-angle engineering in modulating interlayer coupling. Compared with naturally stacked (0°) bilayer WSe_2, in which the intralayer exciton is strongly suppressed and the spectrum is dominated by interlayer emission [15], the twisted sample exhibits a re-emergence of the higher-energy intralayer peak together with a slight redshift of the interlayer emission. This spectral redistribution is consistent with twist-induced modification of interlayer coupling and moiré-driven exciton localization at high-symmetry stacking sites of the moiré lattice [6,20].

3.2. Stark Effect and K-Q Hybrid Interlayer Exciton

To probe the microscopic charge distribution of the interlayer exciton, we measured its energy as a function of the vertical displacement field D while maintaining charge neutrality ($n \approx 0$). Figure 2a shows a false-color contour map of the interlayer exciton PL intensity as a function of photon energy and applied electric field E_z, with the extracted peak positions overlaid as black dots. As E_z is swept from -90 to $+90$ mV/nm, the interlayer exciton peak undergoes a clear and monotonic energy shift in both field directions, providing direct evidence that the interlayer exciton possesses a permanent out-of-plane electric dipole moment.

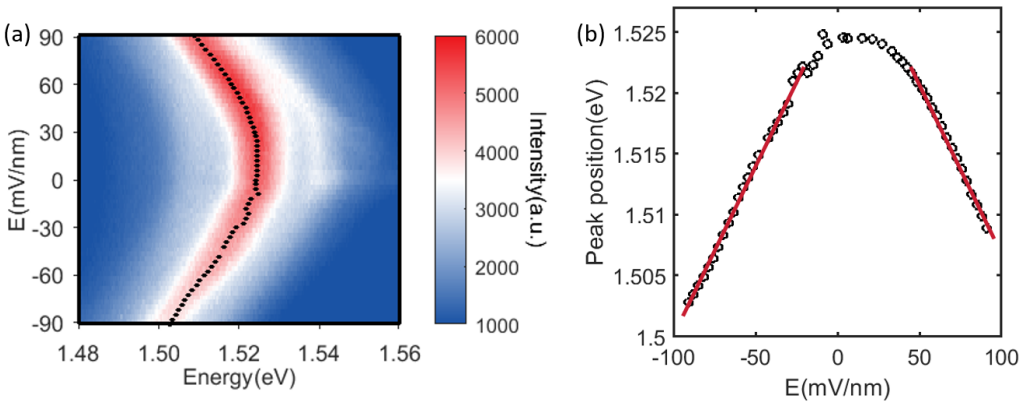


Figure 2. Stark shift of the interlayer exciton in nominal 3° twisted bilayer WSe_2. (**a**) False-color contour plot of the interlayer-exciton photoluminescence intensity as a function of photon energy and effective vertical electric field E_z. (**b**) Extracted interlayer-exciton peak energy as a function of E_z.

Figure 2b plots the extracted interlayer exciton peak energy as a function of E_z. The data exhibit a linear dependence consistent with the first-order Stark effect:

$$\Delta E = e \cdot d \cdot E_z, \tag{4}$$

where ΔE is the exciton energy shift, e is the elementary charge, d is the effective electron–hole separation distance along the out-of-plane direction, and E_z is the applied vertical electric field [14]. A linear fit to the data yields an effective electron–hole separation of $d = 0.26$ nm.

This value is substantially smaller than the physical interlayer spacing in bilayer WSe_2 (∼0.6 nm) and also smaller than the typical charge separation reported for interlayer excitons in large-twist-angle systems (∼0.37 nm) [7]. Such a reduced effective dipole length indicates strong interlayer hybridization. In particular, the conduction-band electron associated with the Q valley is expected to acquire significant interlayer wavefunction delocalization in the small-angle moiré potential, thereby reducing the net charge separation. The extracted Stark shift therefore supports the assignment of the observed interlayer exciton to a K–Q-like hybrid state, distinct from more weakly hybridized layer-indirect excitons in large-angle or naturally stacked bilayers, and is consistent with moiré-modified conduction-band reconstruction in the nominal 3° twisted bilayer WSe_2. Theoretical work by Zhang et al. [21] shows that at a twist angle of 3° in bilayer WSe_2, the K and Q points in momentum space are closest in energy, leading to strong interlayer hybridization. Within this framework, the observed effective electron–hole separation distance d = 0.26 nm can be understood as follows: holes are localized in the K valley, while the wavefunctions of electrons in the Q valley are significantly delocalized across both layers, causing the net charge center to deviate from the midpoint of the interlayer distance.

3.3. Electric-Field Dependence of PL and Valley Polarization

We next examine how the photoluminescence (PL) intensity and the degree of circular polarization (DOCP) evolve with vertical electric field at zero and finite out-of-plane magnetic fields. Figure 3 summarizes these measurements for the nominal 3° twisted bilayer WSe_2.

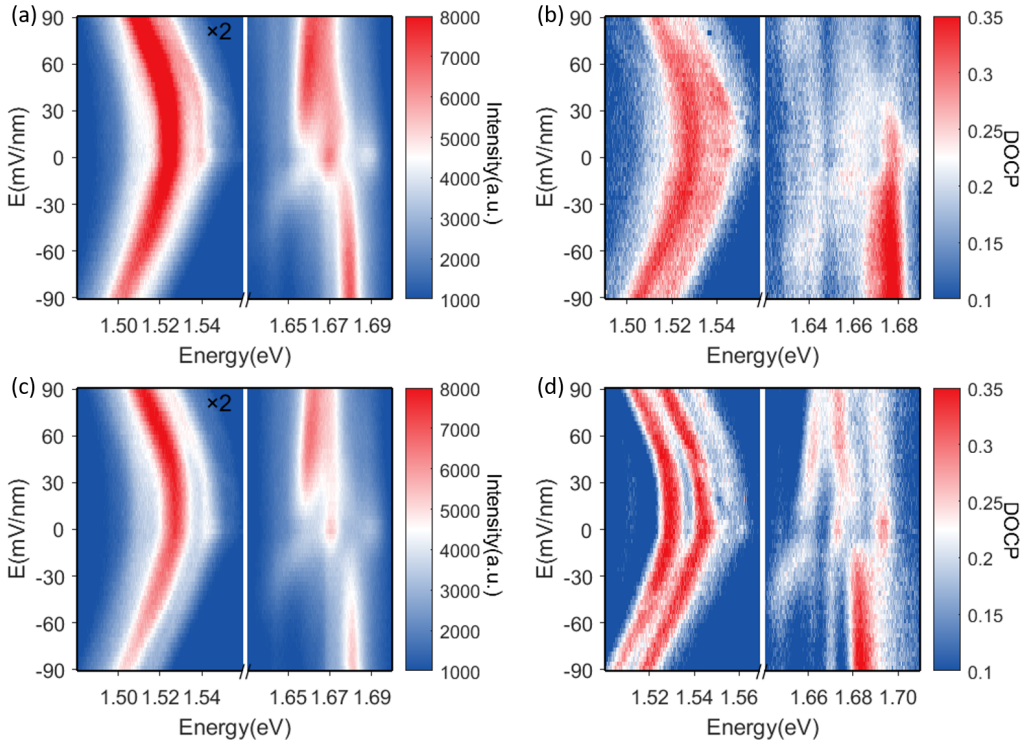


Figure 3. Electric-field dependence of the photoluminescence and degree of circular polarization (DOCP) in nominal 3° twisted bilayer WSe_2. (**a**) PL intensity as a function of emission energy and effective vertical electric field at $B = 0$ T. (**b**) DOCP as a function of emission energy and effective vertical electric field at $B = 0$ T. (**c**) PL intensity as a function of emission energy and effective vertical electric field at $B = 9$ T. (**d**) DOCP as a function of emission energy and effective vertical electric field at $B = 9$ T. The lower-energy spectral window is multiplied by a factor of two in (**a**,**c**), as indicated.

Figure 3a,b show the PL intensity and DOCP, respectively, as a function of vertical electric field at $B = 0$ T. In Figure 3a, the lower-energy interlayer exciton peak (∼1.50–1.54 eV) displays a pronounced Stark shift as E_z is varied, consistent with the results of Figure 2, while the higher-energy intralayer emission (∼1.65–1.69 eV, shown at ×2 intensity scale) shows much weaker field dependence in energy, consistent with the contrasting electric-field responses of interlayer and intralayer excitonic states established in Figure 2. In contrast to the strong energy tunability of the interlayer exciton, the DOCP map in Figure 3b remains comparatively uniform along the interlayer-exciton branch across the entire electric-field range, with no pronounced systematic dependence on E_z within the experimental resolution. This decoupling of energy and polarization responses suggests that the vertical electric field acts primarily on the exciton energy through the Stark effect, while only weakly affecting the valley-polarization response. Although a vertical electric field does deform the exciton wavefunction via the Stark effect, leading to an energy shift, this deformation corresponds to an energy change of only about 20 meV, which is much smaller than the spin–orbit coupling energy of 400 meV. Moreover, the electric field does not break time-reversal symmetry nor alter the spin–valley locking structure between the K and K′ valleys. Consequently, the effect of the electric field on the intervalley scattering rate is expected to be very small. This explains why the DOCP is insensitive to the vertical electric field, while the exciton energy exhibits a significant linear Stark shift.

Figure 3c,d present the corresponding measurements at $B = 9$ T. In Figure 3c, the interlayer exciton continues to display a clear Stark shift with an overall field dependence similar to that at zero field, indicating that the magnetic field does not substantially modify the dipolar characteristic of the interlayer exciton. In Figure 3d, the DOCP again shows only weak dependence on E_z along the interlayer-exciton branch, demonstrating that the decoupling between exciton energy tuning and polarization response remains robust in the presence of a strong magnetic field. Notably, the absolute DOCP level of the interlayer exciton at 9 T appears modestly enhanced relative to the zero-field case, suggesting that although the electric field does not strongly tune the valley polarization, the magnetic field does modify its overall magnitude—a point examined in more detail through the doping-dependent measurements discussed below.

3.4. Doping-Dependent PL and Valley Polarization

We next tune the device electrostatically to examine how the photoluminescence (PL) spectrum and the degree of circular polarization (DOCP) evolve across the electron- and hole-doped regimes. Figure 4 summarizes the doping-dependent PL intensity and DOCP at $B = 0$ T and $B = 9$ T.

Figure 4a,b show the PL intensity and DOCP, respectively, as a function of carrier density at $B = 0$ T. In Figure 4a, as the carrier density is swept across charge neutrality, the PL spectrum evolves from predominantly neutral excitonic emission (X^0) near $n = 0$ to distinct negatively charged (X^-) and positively charged (X^+) excitonic complexes on the electron- ($n > 0$) and hole-doped ($n < 0$) sides, respectively. The interlayer exciton emission is progressively suppressed at high hole doping, reflecting increased non-radiative recombination at large carrier densities. The DOCP map in Figure 4b reveals a pronounced asymmetry between the two doping regimes: on the electron-doped side, the interlayer exciton DOCP is maintained at ∼30%, while on the hole-doped side it is reduced to ∼18%, indicating more efficient valley polarization retention in the electron-doped regime.

This asymmetry can be understood from the spin-valley band structure of bilayer WSe_2. Angle-resolved photoemission spectroscopy measurements [22,23] and density functional theory calculations [15,24] consistently place the conduction band minimum (CBM) at the Q point and the valence band maximum (VBM) at the K point in the natural bilayer.

Our results suggest that these band extrema remain unchanged in the twisted structure, consistent with recent studies on the 3R-stacked bilayer WSe_2 [25]. Valley depolarization of neutral interlayer excitons requires both carriers to scatter with phonons, gain energy, and undergo spin flips [26,27]. In the doped regimes, the depolarization dynamics of charged interlayer excitons are dominated by intervalley scattering [26,28]. In the *n*-doped regime, the negatively charged exciton X^- consists of two electrons distributed across the Q and Q′ valleys and a single hole locked to either the K or K′ valley by strong spin–orbit coupling. Valley depolarization requires this hole to scatter from K to K′; however, owing to the giant spin–orbit splitting of the WSe_2 valence band (∼400 meV) [29], such a spin-flip transition is strongly suppressed, resulting in high valley polarization retention. In the *p*-doped regime, the positively charged exciton X^+ already has holes distributed across both K and K′ valleys, so electron intervalley scattering alone is sufficient in opening a cross-polarization recombination channel, leading to a markedly lower DOCP. The more modest asymmetry observed here (∼30% vs. ∼18%) compared to the dramatic switching (∼80% to <5%) reported by Scuri et al. for a 17° twisted bilayer [7] is attributed to the stronger interlayer coupling at 3° ($d = 0.26$ nm), where an enhanced electron–hole exchange interaction partially counteracts spin-valley locking and moderates the polarization asymmetry.

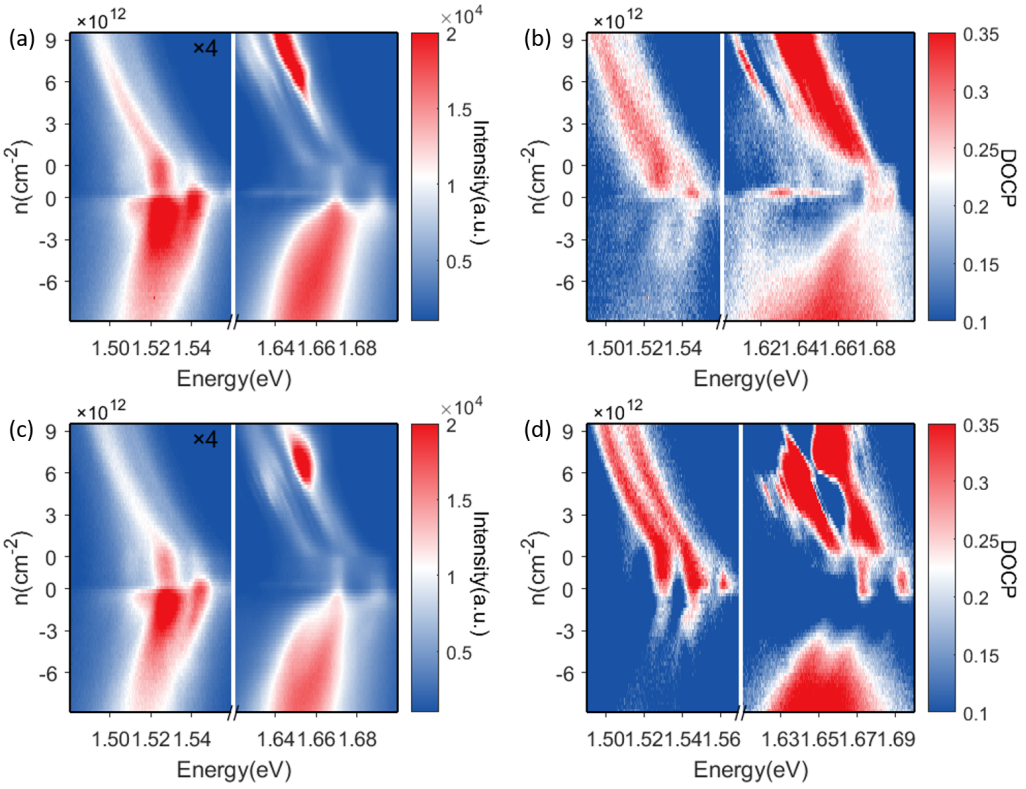


Figure 4. Doping-dependent photoluminescence and degree of circular polarization (DOCP) in nominal 3° twisted bilayer WSe_2. (**a**) PL intensity as a function of emission energy and carrier density at $B = 0$ T. (**b**) DOCP as a function of emission energy and carrier density at $B = 0$ T. (**c**) PL intensity as a function of emission energy and carrier density at $B = 9$ T. (**d**) DOCP as a function of emission energy and carrier density at $B = 9$ T. The lower-energy spectral window is multiplied by a factor of four in (**a**,**c**), as indicated.

Figure 4c,d present the corresponding measurements at $B = 9$ T. The PL spectrum in Figure 4c displays a doping evolution broadly similar to the zero-field case, with X^0, X^-, and X^+ features identifiable across the carrier density range. In Figure 4d, the *n*-/*p*-type DOCP asymmetry becomes more pronounced: the interlayer exciton DOCP increases to

∼35% in the electron-doped regime, while it decreases to ∼13% in the hole-doped regime. We propose that the magnetic field lifts the valley degeneracy via the Zeeman effect. Under 9 T conditions, the Zeeman splitting between the K and K′ valleys reaches the order of meV. The observed changes in DOCP may arise not only from alterations in the scattering dynamics but also from the thermodynamic redistribution of carriers toward the energetically more favorable valley via the Boltzmann effect. Although the microscopic mechanism requires further investigation, the data clearly show that electrostatic doping and the magnetic field act together to control the magnitude and asymmetry of the valley polarization response. These findings reveal the complex interplay between spin dynamics, magnetic field, and carrier doping for interlayer excitons, and further confirm the distinct functional roles of the three external control parameters [18,30]: the vertical electric field primarily tunes exciton energy through the Stark effect, while electrostatic doping and the out-of-plane magnetic field jointly govern the magnitude and asymmetry of the valley polarization.

It should be noted that the DOCP measurements in this work were performed under continuous-wave (CW) conditions; therefore, the DOCP depends on both the total exciton lifetime τ and the spin relaxation time τ_S, following the relation DOCP = $P_0/(1 + \tau/\tau_S)$. Consequently, the observed decrease in DOCP in the hole-doped region may arise partly from changes in τ and partly from changes in τ_S. In the absence of time-resolved PL data, it is currently not possible to quantitatively decouple the contributions of these two factors. We acknowledge this as an inherent limitation of steady-state measurements and suggest that future time-resolved PL measurements be employed to independently determine the evolution of τ and τ_S with doping.

It should be noted that in small-angle twisted bilayers with a twist angle of 3°, lattice reconstruction is inevitable, which leads to strain inhomogeneity and domain structures within the moiré superlattice [18,21]. Such reconstruction may affect the local electronic structure and exciton properties. However, our PL measurements were performed with a relatively large laser spot size (2 µm), which covers many moiré periods (each moiré period is 6 nm, corresponding to approximately 300 periods). Therefore, the observed response is spatially averaged. Despite the presence of local inhomogeneities, the averaged spectra still capture the overall characteristics of the system.

4. Conclusions

Existing studies on the Stark effect or valley polarization of interlayer excitons in twisted WSe_2 have mostly focused on systems with larger twist angles (17°) or natural stacking (0°). In contrast, this work focuses on a small twist angle of 3°—a regime where strong interlayer hybridization and K–Q mixed exciton states are theoretically predicted, but which have not yet been systematically investigated experimentally. Furthermore, while previous works have separately studied the tuning of exciton energies by an electric field, or the effects of doping/magnetic field on valley polarization, this work is the first to simultaneously and independently examine the cooperative and distinct roles of a vertical electric field, electrostatic doping, and an out-of-plane magnetic field on both the energy and valley polarization of interlayer excitons within the same 3° twisted bilayer WSe_2 device. We have investigated interlayer excitons and valley polarization in a nominal 3° twisted bilayer WSe_2 device using low-temperature polarization-resolved photoluminescence spectroscopy under a controlled vertical electric field, electrostatic doping, and an out-of-plane magnetic field. In contrast to natural bilayer WSe_2, where interlayer excitons undergo rapid valley mixing due to the momentum-space alignment of the K and Q valleys, resulting in a degree of circular polarization (DOCP) close to zero [7], our 3° twisted bilayer WSe_2 exhibits significantly enhanced and doping-dependent valley polarization

responses. A pronounced, approximately linear Stark shift of the interlayer exciton yields an effective electron–hole separation of $d = 0.26$ nm, substantially smaller than both the physical interlayer spacing and the separation reported for large-angle twisted systems. This reduced dipole length is consistent with a strongly hybridized K–Q-like intervalley interlayer excitonic state stabilized by the small-angle moiré potential.

Despite the strong electric-field tunability of the exciton energy, the DOCP shows only weak dependence on the vertical electric field at both zero and 9 T magnetic fields, indicating that electric-field tuning acts primarily on the exciton energy through the Stark effect while leaving the valley polarization response largely unaffected. In contrast, electrostatic doping produces a clear asymmetry in valley polarization: at zero magnetic field, the interlayer exciton DOCP is maintained at ∼30% in the electron-doped regime but decreases to ∼18% in the hole-doped regime, consistent with the suppression of hole-mediated intervalley depolarization by the giant spin–orbit splitting (∼400 meV) of the WSe_2 valence band. Under a 9 T out-of-plane magnetic field, this asymmetry is amplified: the DOCP increases to ∼35% on the electron-doped side while decreasing to ∼13% on the hole-doped side, suggesting magnetic-field-modified intervalley depolarization dynamics via Zeeman splitting.

In summary, these results establish a clear functional hierarchy among the external control parameters in nominal 3° twisted bilayer WSe_2: the vertical electric field primarily tunes the exciton energy, whereas electrostatic doping and the magnetic field jointly govern the magnitude and asymmetry of the valley polarization. Our findings deepen the understanding of moiré exciton physics in the small-angle twisted homobilayer regime and establish nominal 3° twisted bilayer WSe_2 as a promising and controllable platform for electrically addressable valley-photonic devices and magnetically tunable spin-valley logic applications. Although this work focuses on a single nominal twist angle (3°), we anticipate that the degree of K–Q hybridization, and consequently the Stark shift and valley polarization asymmetry, will vary continuously with twist angle. A systematic investigation of this angle dependence is an important direction for future research.

Author Contributions: H.Z. conceived the project and designed the devices. H.Z. performed the experiments, data collection, and analysis. H.Z. and K.P. discussed the data and carried out the formal analysis. H.Z. and K.P. jointly wrote, reviewed, and edited the manuscript. All authors have read and agreed to the published version of the manuscript.

Funding: This research received no external funding.

Data Availability Statement: The data that support the findings of this study are available from the corresponding author upon reasonable request.

Acknowledgments: The authors thank the Spin-X Institute, South China University of Technology, for providing necessary experimental facilities.

Conflicts of Interest: The authors declare no conflicts of interest.

References

1. Geim, A.K.; Grigorieva, I.V. Van der Waals heterostructures. *Nature* **2013**, *499*, 419–425. [CrossRef]
2. Novoselov, K.S.; Mishchenko, A.; Carvalho, A.; Castro Neto, A.H. 2D materials and van der Waals heterostructures. *Science* **2016**, *353*, aac9439. [CrossRef] [PubMed]
3. Regan, E.C.; Wang, D.; Paik, E.Y.; Zeng, Y.; Zhang, L.; Zhu, J.; MacDonald, A.H.; Deng, H.; Wang, F. Emerging exciton physics in transition metal dichalcogenide heterobilayers. *Nat. Rev. Mater.* **2022**, *7*, 778–795. [CrossRef]
4. Tran, K.; Choi, J.; Singh, A. Moiré and beyond in transition metal dichalcogenide twisted bilayers. *2D Mater.* **2021**, *8*, 022002. [CrossRef]
5. Yu, H.; Liu, G.B.; Tang, J.; Xu, X.; Yao, W. Moiré excitons: From programmable quantum emitter arrays to spin-orbit coupled artificial lattices. *Sci. Adv.* **2017**, *3*, e1701696. [CrossRef]

6. Andersen, T.I.; Scuri, G.; Sushko, A.; De Greve, K.; Sung, J.; Zhou, Y.; Wild, D.S.; Gelly, R.J.; Heo, H.; Bérubé, D.; et al. Excitons in a reconstructed moiré potential in twisted WSe_2/WSe_2 homobilayers. *Nat. Mater.* **2021**, *20*, 480–487. [CrossRef]
7. Scuri, G.; Andersen, T.I.; Zhou, Y.; Wild, D.S.; Sung, J.; Gelly, R.J.; Bérubé, D.; Heo, H.; Shao, L.; Joe, A.Y.; et al. Electrically tunable valley dynamics in twisted WSe_2/WSe_2 bilayers. *Phys. Rev. Lett.* **2020**, *124*, 217403. [CrossRef]
8. Kim, H.; Lee, G.; Kim, J.; Park, J.; Kim, A.S.; Choi, J.; Watanabe, K.; Taniguchi, T.; Jo, M.H.; Choi, H. Exciton dynamics in marginally twisted WSe_2 homobilayer: Role of interlayer coupling, phonons, and intervalley scattering. *Phys. Rev. B* **2025**, *112*, 104305.
9. Liu, Z.; Gao, Q.; Li, Y.; Espitia, G.; Liu, X.; Shi, C.; Zhang, F.; Kim, D.S.; Ni, Y.; Mackenzie, M.; et al. Field-tunable valley coupling in a dodecagonal semiconductor quasicrystal. *Nat. Phys.* **2026**, *22*, 33–38. [CrossRef]
10. Yu, H.; Yao, W. Luminescence anomaly of dipolar valley excitons in homobilayer semiconductor moiré superlattices. *Phys. Rev. X* **2021**, *11*, 021042. [CrossRef]
11. Balents, L.; Dean, C.R.; Efetov, D.K.; Young, A.F. Superconductivity and strong correlations in moiré flat bands. *Nat. Phys.* **2020**, *16*, 725–733. [CrossRef]
12. Cao, Y.; Fatemi, V.; Fang, S.; Watanabe, K.; Taniguchi, T.; Kaxiras, E.; Jarillo-Herrero, P. Unconventional superconductivity in magic-angle graphene superlattices. *Nature* **2018**, *556*, 43–50. [CrossRef] [PubMed]
13. Cao, Y.; Fatemi, V.; Demir, A.; Fang, S.; Tomarken, S.L.; Luo, J.Y.; Sanchez-Yamagishi, J.D.; Watanabe, K.; Taniguchi, T.; Kaxiras, E.; et al. Correlated insulator behaviour at half-filling in magic-angle graphene superlattices. *Nature* **2018**, *556*, 80–84. [CrossRef]
14. Jauregui, L.A.; Joe, A.Y.; Pistunova, K.; Wild, D.S.; High, A.A.; Zhou, Y.; Scuri, G.; De Greve, K.; Sushko, A.; Yu, C.H.; et al. Electrical control of interlayer exciton dynamics in atomically thin heterostructures. *Science* **2019**, *366*, 870–875. [CrossRef]
15. Wang, Z.; Chiu, Y.H.; Honz, K.; Mak, K.F.; Shan, J. Electrical tuning of interlayer exciton gases in WSe_2 bilayers. *Nano Lett.* **2018**, *18*, 137–143. [CrossRef]
16. Huang, J.; Xiong, Z.; He, J.; Wu, X.; Watanabe, K.; Taniguchi, T.; Lai, S.; Zhang, T.; Han, Z.V.; Zhao, S. Electrically tunable Γ–Q interlayer excitons in twisted $MoSe_2$ bilayers. *J. Mater. Sci. Technol.* **2025**, *207*, 70–75.
17. Huang, Z.; Zhao, Y.; Bo, T.; Chu, Y.; Tian, J.; Liu, L.; Yuan, Y.; Wu, F.; Zhao, J.; Xian, L.; et al. Spatially indirect intervalley excitons in bilayer WSe_2. *Phys. Rev. B* **2022**, *105*, L041409.
18. Sevik, C.; Torun, E.; Milosevic, M.V.; Paleari, F. State- and momentum-dependent nonlinear Stark effect of interlayer excitons in bilayer WSe_2. *Nano Lett.* **2025**, *25*, 9918–9927. [CrossRef]
19. Kormányos, A.; Zólyomi, V.; Fal'ko, V.I.; Burkard, G. Tunable Berry curvature and valley and spin Hall effect in bilayer MoS_2. *Phys. Rev. B* **2018**, *98*, 035408.
20. Seyler, K.L.; Rivera, P.; Yu, H.; Wilson, N.P.; Ray, E.L.; Mandrus, D.G.; Yan, J.; Yao, W.; Xu, X. Signatures of moiré-trapped valley excitons in $MoSe_2/WSe_2$ heterobilayers. *Nature* **2019**, *567*, 66–70. [CrossRef]
21. Zhang, Z.; Wang, Y.; Watanabe, K.; Taniguchi, T.; Ueno, K.; Tutuc, E.; LeRoy, B.J. Flat bands in twisted bilayer transition metal dichalcogenides. *Nat. Phys.* **2020**, *16*, 1093–1096. [CrossRef]
22. Sie, E.J.; Rohwer, T.; Lee, C.; Gedik, N. Time-resolved XUV ARPES with tunable 24–33 eV laser pulses at 30 meV resolution. *Nat. Commun.* **2019**, *10*, 3535. [CrossRef]
23. Nguyen, P.V.; Teutsch, N.C.; Wilson, N.P.; Kahn, J.; Xia, X.; Graham, A.J.; Kandyba, V.; Giampietri, A.; Barinov, A.; Constantinescu, G.C.; et al. Visualizing electrostatic gating effects in two-dimensional heterostructures. *Nature* **2019**, *572*, 220–223. [CrossRef] [PubMed]
24. Liu, G.B.; Xiao, D.; Yao, Y.; Xu, X.; Yao, W. Electronic structures and theoretical modelling of two-dimensional group-VIB transition metal dichalcogenides. *Chem. Soc. Rev.* **2015**, *44*, 2643–2663. [CrossRef]
25. Du, L.; Zhang, Q.; Zhang, T.; Jia, Z.; Liang, J.; Liu, G.B.; Yang, R.; Shi, D.; Xiang, J.; Liu, K.; et al. Robust circular polarization of indirect QK transitions in bilayer 3R-WS_2. *Phys. Rev. B* **2019**, *100*, 161404. [CrossRef]
26. Wang, G.; Chernikov, A.; Glazov, M.M.; Heinz, T.F.; Marie, X.; Amand, T.; Urbaszek, B. Colloquium: Excitons in atomically thin transition metal dichalcogenides. *Rev. Mod. Phys.* **2018**, *90*, 021001. [CrossRef]
27. Singh, A.; Tran, K.; Kolarczik, M.; Seifert, J.; Wang, Y.; Hao, K.; Pleskot, D.; Gabor, N.M.; Helmrich, S.; Owschimikow, N.; et al. Long-lived valley polarization of intravalley trions in monolayer WSe_2. *Phys. Rev. Lett.* **2016**, *117*, 257402. [CrossRef]
28. Mak, K.F.; Xiao, D.; Shan, J. Light–valley interactions in 2D semiconductors. *Nat. Photonics* **2018**, *12*, 451–460. [CrossRef]
29. Aivazian, G.; Gong, Z.; Jones, A.M.; Chu, R.L.; Yan, J.; Mandrus, D.G.; Zhang, C.; Cobden, D.; Yao, W.; Xu, X. Magnetic control of valley pseudospin in monolayer WSe_2. *Nat. Phys.* **2015**, *11*, 148–152. [CrossRef]
30. Wang, X.; Zhu, J.; Seyler, K.L.; Rivera, P.; Zheng, H.; Wang, Y.; He, M.; Taniguchi, T.; Watanabe, K.; Yan, J.; et al. Moiré trions in $MoSe_2/WSe_2$ heterobilayers. *Nat. Nanotechnol.* **2021**, *16*, 1208–1213. [CrossRef]

Disclaimer/Publisher's Note: The statements, opinions and data contained in all publications are solely those of the individual author(s) and contributor(s) and not of MDPI and/or the editor(s). MDPI and/or the editor(s) disclaim responsibility for any injury to people or property resulting from any ideas, methods, instructions or products referred to in the content.